carbides. The multiphase/polytypic region can be expected to occur also in the nitrides because the electronic structure of the nitrides is generally very similar to that of the carbides, with only simple rigid band shifts. Boxman and coworkers also report a substantial increase of hardness (from 25 GPa up to 50 GPa) in $Ti_xNb_{1-x}N$ for x slightly below 0.5 (*23*).

In conclusion, we have identified regions in valence electron concentration where several phases of the 3d, 4d, and 5d transition metal carbides have the same or similar total energies. From this finding, we suggest that compounds may be deposited, using modern thin-film techniques, where the stacking sequence of atomic layers is essentially random or controllable through minor changes of the production parameters. Further experimental studies of the proposed systems are highly desired. Examples of possible embodiments include coatings deposited at the calculated optimum VEC, where several structures have the same energies, with essentially random stacking sequences or a large number of stacking faults. A second alternative is one where layers of two alternating structures are deposited, by controlled variations in deposition conditions, creating superlattices differing only in structure but not in chemical composition. The multiphase/polytypic regions and the consequent hardening mechanism predicted here are also expected to be found in other systems, for example, the transition metal nitrides. The hardness of, for example, coatings from such multiphase/polytypic, or stacking-fault–rich, compounds with a large number of different glide-systems suppressing the propagation of dislocations is predicted to be substantially enhanced over that of traditional transition metal carbide/nitride coatings.

References and Notes

1. S. A. Barnett, A. Madan, *Phys. World* (January 1998), p. 45.
2. U. Helmersson, S. Todorova, S. A. Barnett, J.-E. Sundgren, *J. Appl. Phys.* **62**, 481 (1987).
3. L. Hultman *et al.*, *Z. Metallkde.* **90**, 803 (1999).
4. H. J. Goldschmidt, *Interstitial Alloys* (Butterworths, London, 1967).
5. L. E. Toth, *Transition Metal Carbides and Nitrides* (Academic Press, New York, 1971).
6. C. Maerky, M.-O. Guillou, J. L. Henshall, R. M. Hooper, *Mat. Sci. Eng.* **A209**, 329 (1996).
7. K. Schwarz, *CRC Crit. Rev. Solid State Mat. Sci.* **13**, 211 (1987).
8. L. I. Johansson, *Surf. Sci. Rep.* **21**, 177 (1995).
9. J. Redinger *et al.*, *J. Phys. Chem. Solids* **46**, 383 (1985).
10. A. Y. Liu, R. M. Wentzcovitch, M. L. Cohen, *Phys. Rev. B* **38**, 9483 (1988).
11. D. L. Price, B. R. Cooper, *Phys. Rev. B* **39**, 4945 (1989).
12. S. H. Jhi, J. Ihm, S. G. Louie, M. L. Cohen, *Nature* **399**, 132 (1999).
13. H. W. Hugosson *et al.*, *J. Appl. Phys.* **86**, 7 3758 (1999).
14. L. Norin, H. Högberg, J. Lu, J. O. Malm, U. Jansson, *Appl. Phys. Lett.* **73**, 2754 (1998).
15. A. Kelly, N. H. MacMillan, *Strong Solids* (Clarendon, Oxford, 1986).
16. G. Kresse, J. Hafner, *Phys. Rev. B* **47**, 558 (1993).
17. G. Kresse, J. Furthmüller, *Phys. Rev. B* **55**, 11169 (1996).
18. The exchange-correlation functional according to Ceperley and Adler, as parameterized by Perdew and Zunger, is used in all calculations presented here. The calculations have been performed with ultrasoft Vanderbilt-type pseudopotentials. The plane wave cutoff was 600 eV. The k points were obtained with a Monkhorst-Pack method, and a k point grid of 8 by 8 by 8 was chosen for all structures ensuring convergence with respect to k points.
19. For the 4d TMCs, the results from the pseudopotential plane wave method were also compared with those from a more accurate full-potential method where the Kohn-Sham equation is solved without making approximations for the shape of the effective potential or to the charge density (*24*). Comparing the energies obtained from the two methods, the phase stability differences were found to be very similar, varying within 10%.
20. T. Y. Velikanova, V. Z. Kublii, B. V. Khaenko, *Sov. Powder Metall. Metal Ceram.* **27**, 891 (1988).
21. An increase in stacking fault density has also been seen in transmission electron microscopy studies of γ'-$MoC_{0.74}$; J. Lu, H. W. Hugosson, O. Eriksson, L. Nordström, U. Jansson, *Thin Solid Films* **370**, 203 (2000).
22. O. Knotek, A. Barimani, B. Bosserhoff, L. Löffler, *Thin Solid Films* **193–194**, 557 (1990).
23. R. L. Boxman *et al.*, *Surf. Coat. Technol.* **125**, 257 (2000).
24. J. M. Wills, O. Eriksson, M. Alouani, D. L. Price, in *Electronic Structure and Physical Properties of Solids*, H. Dreysse, Ed. (Springer-Verlag, Berlin, 2000), pp. 148–167.

25. This work has been supported by the Swedish Research Council (NFR and TFR) and the Swedish Foundation for Strategic Research (SSF). The authors wish to acknowledge J. M. Wills for supplying the FP-LMTO code and the support of S. Mirbt in the parts of the study using the VASP code. Valuable discussions with J.-P. Palmquist, L. Hultman, and S. G. Louie are also acknowledged. All rights to the invention detailed in this study are protected within the patent application Patentverket 0004203-6 (2000).

8 March 2001; accepted 23 August 2001

Stability and Structure of $MgSiO_3$ Perovskite to 2300-Kilometer Depth in Earth's Mantle

Sang-Heon Shim,[1]*† Thomas S. Duffy,[1] Guoyin Shen[2]

Unexplained features have been observed seismically near the middle (~1700-kilometer depth) and bottom of the Earth's lower mantle, and these could have important implications for the dynamics and evolution of the planet. (Mg,Fe)SiO_3 perovskite is expected to be the dominant mineral in the deep mantle, but experimental results are discrepant regarding its stability and structure. Here we report in situ x-ray diffraction observations of (Mg,Fe)SiO_3 perovskite at conditions (50 to 106 gigapascals, 1600 to 2400 kelvin) close to a mantle geotherm from three different starting materials, $(Mg_{0.9}Fe_{0.1})SiO$ enstatite, $MgSiO_3$ glass, and an $MgO+SiO_2$ mixture. Our results confirm the stability of (Mg,Fe)SiO_3 perovskite to at least 2300-kilometer depth in the mantle. However, diffraction patterns above 83 gigapascals and 1700 kelvin (1900-kilometer depth) cannot presently rule out a possible transformation from *Pbnm* perovskite to one of three other possible perovskite structures with space group $P2_1/m$, *Pmmn*, or $P4_2/nmc$.

Knowledge of the phase relations and crystal structures of lower mantle materials are essential for evaluating seismic observations (*1–3*) of the deep mantle and their geochemical and geodynamic implications (*2*, *4*). The stability and structure of (Mg,Fe)SiO_3 perovskite have been controversial over the last decade. Knittle and Jeanloz (*5*) confirmed the stability of orthorhombic (Mg,Fe)SiO_3 perovskite to 127 GPa using x-ray diffraction (XRD) on temperature-quenched samples. However, Meade *et al.* (*6*) reported observation of an orthorhombic-to-cubic phase transformation and dissociation to $(Mg,Fe)O+SiO_2$ on the basis of XRD studies of laser-heated samples at 60 to 70 GPa. The dissociation reaction was supported by Saxena *et al.*, who performed diffraction studies on both temperature-quenched (*7*) and high-temperature (*8*) samples laser heated at 60 to 90 GPa. In contrast, Raman measurements on temperature-quenched samples (*9*) and XRD measurements on laser-heated samples (*10*, *11*) were reported to show the stability of orthorhombic $MgSiO_3$ perovskite at these conditions. The origin of the discrepancy between these results remains controversial (*13*, *14*). The primary issues include the homogeneity of heating, stress conditions, transformation kinetics, and the possibility of chemical reactions.

The structure of SiO_2 at lower mantle conditions is also important, not only because of the possible existence of free silica in the mantle but also because of its effect on the relative stability

[1]Department of Geosciences, Princeton University, Princeton, NJ 08544, USA. [2]CARS, University of Chicago, Chicago, IL 60637, USA.

*To whom correspondence should be addressed. E-mail: sangshim@uclink.berkeley.edu

†Present address: Department of Earth and Planetary Science, University of California, Berkeley, CA 94720–4767, USA.

between $MgO+SiO_2$ and $MgSiO_3$ perovskite. A post-stishovite phase was reported to have the $CaCl_2$ structure (*15*) above 54 GPa. Dubrovinsky *et al.* (*16*, *17*) proposed an additional phase transformation from $CaCl_2$ to α-PbO_2 phase above 80 GPa. However, in another study (*18*), the stability of the $CaCl_2$ phase was confirmed up to 120 GPa on temperature-quenched samples.

Here, three different materials were used to study the stability of $(Mg,Fe)SiO_3$ perovskite: $(Mg_{0.9}Fe_{0.1})SiO_3$ enstatite, pure $MgSiO_3$ glass, and an equi-molar $MgO+SiO_2$ mixture. Pure starting materials were mixed with 10 weight percent (wt%) platinum, which serves as both an internal pressure standard and a laser absorber. Pressure was determined using the equations of state of platinum (*19*) and argon (*20*). The calculated pressure uncertainties are 4 to 15 GPa, due mainly to the effect of overlaps between platinum and argon diffraction lines at 70 to 100 GPa but also due to shear stresses and temperature uncertainty. A 10-μm thick foil of the sample mixture was loaded in a 50-μm hole in a rhenium gasket and was compressed in a symmetric diamond cell by 100-μm beveled anvils for experiments above 70 GPa. The sample was loaded in a 150-μm hole in a stainless steel gasket and was compressed by 300-μm diamond anvils for experiments below 60 GPa. Argon was cryostatically loaded as a pressure-transmitting and insulation medium. For experiments below 60 GPa, NaCl was used as the pressure medium.

In situ laser heating and XRD measurements were conducted at the GeoSoilEnviroCARS (GSECARS) sector of the Advanced Photon Source (*21*). Temperature was determined by fitting the thermal radiation spectra, corrected for system response, to Planck's equation (Web fig. 1 is available at *Science* Online at www.sciencemag.org/cgi/content/full/293/5539/2437/DC1). The mean temperature over the x-rayed volume was obtained by a three-dimensional averaging technique (*22*). The temperature uncertainty (1σ) was 100 to 250 K in these experiments including radial and axial thermal gradients, the effect of temperature fluctuation during the x-ray exposure, and the fitting residual. Diffraction patterns were measured with the use of energy-dispersive techniques and a solid state detector (*23*).

For phase identification, we calculated expected diffraction peak positions and their intensities for $MgSiO_3$ perovskite, MgO, and SiO_2 phases. Structural parameters for $MgSiO_3$ perovskite were obtained from recent high-pressure and -temperature (P-T) x-ray measurements (*10*). For SiO_2, we calculated diffraction patterns for all the phases proposed by experiments (*16*, *18*) and a first principles calculation (*24*), including the $CaCl_2$ and α-PbO_2 structures. Pressure and temperature variation of lattice spacings were determined using the equations of state of $MgSiO_3$ perovskite (*10*) and MgO (*25*). For SiO_2 phases we assume that the equations of state of all high-pressure forms are the same as stishovite (*26*).

For each run, the pressure was increased directly to 60 to 100 GPa, and then heating was performed while diffraction patterns were recorded (Fig. 1). The typical duration of a heating run is ~30 min. New features, which can be assigned as silicate perovskite diffraction peaks, appeared in patterns immediately after the lasers began to irradiate the starting materials. The dominant features in the observed patterns can be explained by the existence of silicate perovskite during and after the first heating for all three starting materials. The observed peak positions agree with recent in situ XRD measurements at similar P-T conditions (*10*) (Fig. 1). We also performed more heating cycles on these transformed $MgSiO_3$ perovskite samples; no evidence for dissociation to $MgO+SiO_2$ was found. These heating runs cover pressures of 50 to 106 GPa and temperatures of 1600 to 2400 K (Figs. 1 and 2). In another words, $MgSiO_3$ perovskite features were consistently observed upon heating $(Mg,Fe)SiO_3$ enstatite, $MgSiO_3$ glass, $MgO+SiO_2$ mixture, and $MgSiO_3$ perovskite under in situ high P-T conditions and upon temperature quench. It is notable that the P-T conditions of our observations are close to the expected geotherm for the lower mantle (Fig. 2).

Due to the limited resolution of the energy dispersive technique and the weak diffraction from silicate samples above 70 GPa, we were not able to resolve all lines for the doublets of *Pbnm* perovskite, 002+110, and 103+211. For triplets, oscillation of the diamond anvil cell (DAC) during the measurements enables us to resolve two or three distinct lines below 78 GPa (Fig. 1A). This indicates that $MgSiO_3$ perovskite has an orthorhombic unit cell and that no phase transformation to a higher symmetry phase (tetragonal or cubic) exists to 78 GPa.

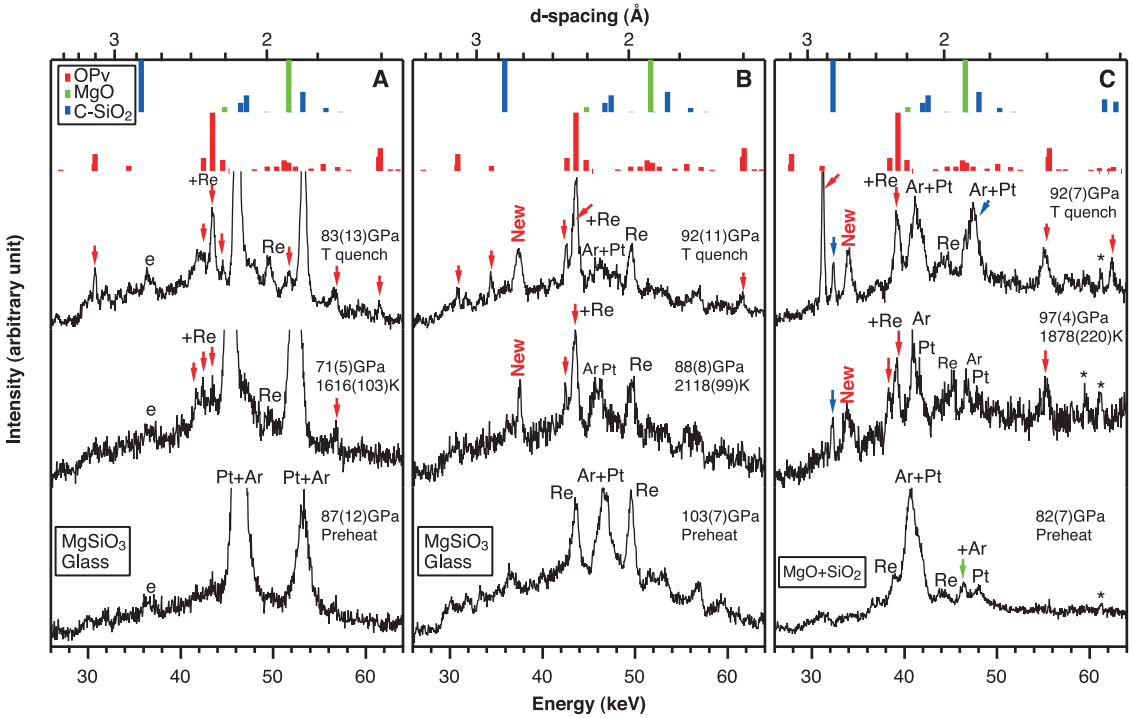

Fig. 1. Representative XRD patterns at the indicated P-T conditions. Calculated patterns for the indicated P-T conditions for orthorhombic *Pbnm* perovskite (red) based on the structural parameters measured at 79.7 GPa and 1681 K(*10*), periclase (green), and $CaCl_2$-type SiO_2 (blue) are shown at the top. Peak identification is presented for each diffraction line (red arrows, $MgSiO_3$ perovskite; blue arrows, $CaCl_2$ type SiO_2; green arrows, periclase; New, possible new perovskite line; Pt, platinum; Ar, argon; Re, rhenium; asterisk, x-ray fluorescence; e, escape peak. Starting materials are given with the x-ray diffraction patterns before heating. (**A**) $MgSiO_3$ glass → $MgSiO_3$ perovskite (*Pbnm*) below 88 GPa. (**B**) $MgSiO_3$ glass → $MgSiO_3$ perovskite plus new line. (**C**) $MgO+SiO_2$ → $MgSiO_3$ perovskite plus new line (*32*).

A new peak (d-spacing ≅ 2.62 Å) was found above 88 GPa in patterns that also contained lines attributable to *Pbnm* perovskite both during and after heating runs (Fig. 1, B and C). This line was observed in ~50% of measured diffraction patterns during the first heating runs and appeared at specific rotation angles of the DAC, which implies considerable preferred orientation or crystal growth. This feature was detected for two different starting materials, $MgSiO_3$ glass and $MgO+SiO_2$, and was also found upon subsequent heating of material already transformed to $MgSiO_3$ perovskite, although, in the latter case, the new line is only rarely seen (2 out of 23 diffraction patterns). In addition, the position of this new line is pressure- and temperature-dependent. Calculated XRD patterns (Fig. 1, B and C) showed that this line cannot be from MgO, the $CaCl_2$ phaseof SiO_2, or any other of theoretically proposed post-stishovite phases (*24*) including α-PbO_2. In fact, this line can be indexed as 012 using the unit-cell parameters of the *Pbnm* orthorhombic cell, but this line is systematically absent from this space group. The appearance of a new peak while retaining *Pbnm* perovskite features could indicate a phase transformation to another perovskite structure.

Most perovskite phase transformations are induced by tilting of rigid octahedral units (i.e., SiO_6 in $MgSiO_3$ perovskite) with respect to the three pseudo-cubic axes (*27*, *28*). Such a geometrical model can be used to determine all possible space groups for this structure. We used the following constraints from our observation to investigate possible structures allowed by this model; first, one singlet (111), two doublets (002+110 and 103+211), and one triplet (020+112+200) of *Pbnm* should be retained. However, because we were able to observe only one of the doublets and two of the triplets above 88 GPa, we also allow fewer lines. Second, a space group should allow a line at 2.62 Å. By consideration of the systematic absence rule for possible perovskite structures, we find that only three space groups can satisfy all of these constraints: $P2_1/m$ (monoclinic), *Pmmn* (orthorhombic), and $P4_2/nmc$ (tetragonal).

Direct structure determination is not possible from energy-dispersive XRD patterns at these extreme conditions because of unreliable line intensities. Instead, we compare our observation with calculated diffraction patterns of these three possible space groups. According to our observation, the new feature at 2.62 Å should be more intense compared with other lines (Fig. 1, B and C). It is necessary to know atomic positions to calculate the relative intensities of individual XRD lines. Atomic positions can be calculated using unit-cell parameters, tilting angles, and a geometrical model. However, the model does not provide the position shifts of the cations from the dodecahedral site centers and the distortion of octahedra, which are also the important contributors to the intensity. We performed a first-order calculation using the POTATO (*28*) and GSAS (*29*) packages by ignoring these factors (Table 1). The calculated intensities for the three candidates are all within the observed intensity range. Interestingly, a recent first principles calculation also proposed a possible phase transformation of $MgSiO_3$ perovskite from *Pbnm* to *Pmmn* at 70 to 140 GPa and 2000 to 3000 K (*30*).

The $P2_1/m$ phase [$a^+b^-c^-$ in Glazer's notation (*27*)] can be achieved by changing the tilting angles of *Pbnm* phase ($a^+b^-b^-$) along *b* and *c* pseudo-cubic axes (Fig. 3A). Instead, $P4_2/nmc$ ($a^+a^+c^-$) and *Pmmn* ($a^+b^+c^-$) have different tilting senses from *Pbnm* and $P2_1/m$ (Fig. 3B). These differences result in different tilts between alternating octahedra layers in a perovskite structure: *Pbnm* and $P2_1/m$ have the same tilting senses for the layers along one of the pseudo-cubic axes but $P4_2/nmc$ and *Pmmn* have these layers for two of the pseudo-cubic axes (Fig. 3). Such structural differences could lead to differences in elastic properties that may be seismically detectable (*30*). However, further investigation is needed to better define the crystal structure and its relation to physical properties.

Using the $MgO+SiO_2$ starting material, we observed a SiO_2 diffraction line originating from excess silica in the mixture, or nonstoichiometry of the synthesized perovskite during and after heating, together with $MgSiO_3$ perovskite features. Our observations are consistent with the $CaCl_2$ type rather than the α-PbO_2 type at 94 to 106 GPa and 1675 to 2010 K (Fig. 1C).

All other observed lines could be explained by sample materials, pressure media, gasket, fluorescence lines, or detector escape peak except for a single line at 2.38 Å that could not be attributed to any perovskite structure or SiO_2 phase. For example, the most intense line of the α-PbO_2 form of SiO_2 could explain this line only if the pressure was overestimated by 30 GPa from the value measured using the pressure standards and $MgSiO_3$ perovskite. Because this line was observed in only one of our four experiments, we have not considered it further.

Our results can also address the origin of discrepancy between recent Raman (*9*) and XRD (*10*, *18*) studies and those of Meade *et al.* (*6*), Saxena *et al.* (*7*, *8*), and Dubrovinsky *et al.* (*16*, *17*) regarding the stability of $MgSiO_3$ perovskite and the structure of SiO_2. Unlike previous work, our measurements were performed at in situ conditions with the use of an inert pressure medium (Ar), which prevents reaction between the pressure medium and sample and also avoids an extreme thermal gradient by insulating the sample from the diamond anvils. Also, we use an advanced laser-heating technique that provides a large homogeneous heating spot using the TEM_{01} mode of Nd:YLF (Nd doped $LiYF_4$)/laser and double-sided heating (*31*). We believe

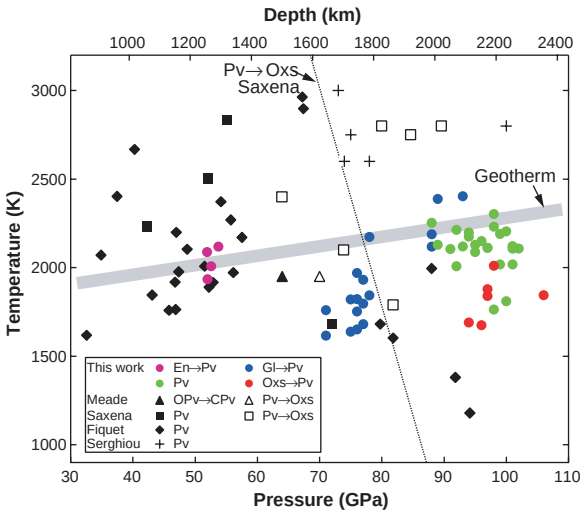

Fig. 2. Pressure-temperature conditions for silicate perovskite experiments. Open symbols are data points obtained using in situ XRD where the dissociation of $(Mg,Fe)SiO_3$ perovskite was reported [open triangles, Meade *et al.* (*6*); open squares, Saxena *et al.* (*8*)]. Solid symbols are data points obtained using in situ XRD where the stability of $(Mg,Fe)SiO_3$ perovskite was confirmed [solid squares, Saxena *et al.* (*8*); solid diamonds, Fiquet *et al.* (*33*, *10*); colored solid circles, this work]. A solid triangle shows the P-T conditions where Meade *et al.* (*6*) reported a phase transformation from orthorhombic (OPv) to cubic (CPv) perovskite. Colors indicate different starting materials for this work [purple, $(Mg,Fe)SiO_3$ enstatite (En); blue, $MgSiO_3$ glass (Gl); green, $MgSiO_3$ perovskite (Pv); red, $MgO+SiO_2$ (Oxs)]. Crosses are from Raman observations of temperature-quenched samples (*9*). The gray region shows the approximate location of the mantle geotherm (*12*). The dotted line is the tentative boundary between $MgSiO_3$ perovskite and $MgO+SiO_2$ reported by Saxena *et al.* (*8*).

Table 1. Calculated XRD intensity of the 2.62 Å line, ignoring octahedra distortion and cation shift from the dodecahedral site center and the number of lines contributing to the intensity for different space groups. Observed intensity range is also shown for comparison.

Space group	I/I_0 (%)	No. of lines
$P2_1/m$	5	2
$P4_2/nmc$	27	2
Pmmn	5	3
Pbnm (*10*)	0	0
Observation	5 to 20	

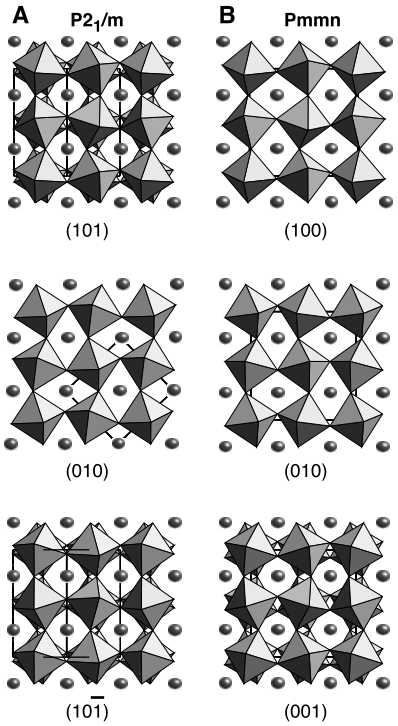

Fig. 3. Possible crystal structures of $MgSiO_3$ perovskite above 83 GPa. (**A**) $P2_1/m$ and (**B**) *Pmmn*. Projections along pseudo-cubic axes are shown for comparison. The crystal structures of $P2_1/m$ and *Pmmn* have same tilting senses as *Pbnm* and $P4_2/nmc$, respectively. The unit cell is shown by solid lines.

these technical improvements provide a better sample environment for examining the stability of $MgSiO_3$ perovskite and the structure of SiO_2 at extreme conditions.

Although two earlier quench studies (*9*, *11*) and one in situ study (*10*) performed above 88 GPa reported the existence of $MgSiO_3$ perovskite, none of them reported the new diffraction feature we observed. Serghiou *et al.* (*9*) used Raman spectroscopy for phase identification on quenched samples. Because the phase transformation is expected to be subtle, the Raman study, which relied on only a few major Raman features, may not have been able to detect this change. Fiquet *et al.* (*10*) performed in situ angle-dispersive XRD measurements but their P-T conditions are generally lower than ours (Fig. 2). Andrault (*11*) studied aluminum- and iron-bearing $MgSiO_3$ perovskite samples that were heated for a few seconds. The lack of observation of new features in these studies indicates that further examination of possible perovskite structure is needed before any further conclusions can be drawn. The presence of a small but highly oriented unknown impurity phase can, for example, produce unexplained lines in an XRD pattern. Our observation that the new line is only rarely seen upon further heating of transformed perovskite samples indicates that preferred orientation and metastability may also be important factors.

The principal result of this study confirms the stability of $(Mg,Fe)SiO_3$ perovskite to 2300-km depth conditions using in situ XRD measurements and homogeneous laser heating in both the radial and axial directions. It is also found that the structure of SiO_2 is the $CaCl_2$ type at pressures equivalent to 2400-km depth. Above 88 GPa, we observed the appearance of a new peak together with *Pbnm* $MgSiO_3$ perovskite features. One possible explanation for this feature is transformation of *Pbnm* perovskite to one of three other perovskite structures.

References and Notes

1. R. D. van der Hilst, H. Kárason, *Science* **283**, 1885 (1999).
2. T. Lay, Q. Williams, E. J. Garnero, *Nature* **392**, 461 (1998).
3. I. Sidorin, M. Gurnis, D. V. Helmberger, *Science* **286**, 1326 (1999).
4. L. H. Kellogg, B. H. Hager, R. D. van der Hilst, *Science* **283**, 1881 (1999).
5. E. Knittle, R. Jeanloz, *Science* **235**, 668 (1987).
6. C. Meade, H.-K. Mao, J. Hu, *Science* **268**, 1743 (1995).
7. S. K. Saxena *et al.*, *Science* **274**, 1357 (1996).
8. S. K. Saxena, L. S. Dubrovinsky, P. Lazor, J. Z. Hu, *Eur. J. Mineral.* **10**, 1275 (1998).
9. G. Serghiou, A. Zerr, R. Boehler, *Science* **280**, 2093 (1998).
10. G. Fiquet *et al.*, *Geophys. Res. Lett.* **27**, 21 (2000).
11. D. Andrault, *J. Geophys. Res.* **106**, 2079 (2001).
12. J. M. Brown, T. J. Shankland, *Geophys. J. R. Astron. Soc.* **66**, 576 (1981).
13. L. S. Dubrovinsky, S. K. Saxena, S. Rekhi, *Science*, 13 August 1999 (www.sciencemag.org/cgi/content/full/285/5430/983a).
14. G. Serghiou, A. Zerr, R. Boehler, *Science*, 13 August 1999 (www.sciencemag.org/cgi/content/full/285/5430/983a).
15. K. J. Kingma, R. E. Cohen, R. J. Hemley, H.-K. Mao, *Nature* **374**, 243 (1995).
16. L. S. Dubrovinsky *et al.*, *Nature* **388**, 362 (1997).
17. L. S. Dubrovinsky *et al.*, *Chem. Phys. Lett.* **333**, 264 (2001).
18. D. Andrault, G. Fiquet, F. Guyot, M. Hanfland, *Science* **282**, 720 (1998).
19. N. C. Holmes, J. A. Moriarty, G. R. Gathers, W. J. Nellis, *J. Appl. Phys.* **66**, 2962 (1989).
20. L. W. Finger *et al.*, *Appl. Phys. Lett.* **39**, 892 (1981).
21. The laser-heating system (*31*) at GSECARS uses a TEM_{01} Nd:YLF laser, which provides a radially homogeneous temperature profile over 20 μm. Separate laser paths for each side of the sample reduces the axial thermal gradient, while separate imaging spectrometers enable us to measure the temperature profiles from both sides with a spatial resolution of 1.7 μm.
22. S.-H. Shim, T. S. Duffy, G. Shen, *J. Geophys. Res.* **105**, 25955 (2000).
23. A small horizontally focused x-ray beam was used (5 μm by 8 μm) to minimize the temperature inhomogeneity in the x-ray probed area. In order to reduce the effect of preferred crystallographic orientation at high temperature, the diamond anvil cell was oscillated by ±20° about its loading axis during the x-ray measurement. Alignment techniques ensured the co-linearity of the incident lasers, x-ray beam, and diamond cell rotation axis.
24. D. M. Teter, R. J. Hemley, G. Kresse, J. Hafner, *Phys. Rev. Lett.* **80**, 2145 (1998).
25. S. Speziale *et al.*, *J. Geophys. Res.* **106**, 515 (2001).
26. R. J. Hemley, C. T. Prewitt, K. J. Kingma, in *Silica: Physical Behavior, Geochemistry and Material Applications*, P. J. Heaney, C. T. Prewitt, G. V. Gibbs, Eds. (Mineralogical Society of America, Washington, DC, 1994), pp. 41–82.
27. A. M. Glazer, *Acta Crystallogr.* **B28**, 3384 (1972).
28. P. M. Woodward, *Acta Crystallogr.* **B53**, 32 (1997).
29. A. C. Larson, R. B. V. Dreele, Tech. Rep. LAUR 86-748, Los Alamos National Laboratory (1988).
30. B. Kiefer, L. Stixrude, *Eos* **81**, S55 (2000).
31. G. Shen, M. L. Rivers, Y. Wang, S. R. Sutton, *Rev. Sci. Instrum.* **72**, 1273 (2001).
32. Rhenium gasket lines arise from low-intensity (~1%) x-ray tails, which are incompletely removed by a secondary ("clean-up") slit system (*31*).
33. G. Fiquet *et al.*, *Phys. Earth Planet. Interiors* **105**, 21 (1998).

34. We thank S. Speziale and S. Shieh for experimental assistance, J. Akins and T. J. Ahrens for providing glass starting material, and P. M. Woodward and A. Kavner for helpful discussion. Supported by the NSF and the Packard foundation. Use of the Advanced Photon Source was supported by the DOE.

2 April 2001; accepted 17 August 2001

ENSO-like Forcing on Oceanic Primary Production During the Late Pleistocene

Luc Beaufort,[1] Thibault de Garidel-Thoron,[1] Alan C. Mix,[2] Nicklas G. Pisias[2]

Late Pleistocene changes in oceanic primary productivity along the equator in the Indian and Pacific oceans are revealed by quantitative changes in nanoplankton communities preserved in nine deep-sea cores. We show that variations in equatorial productivity are primarily caused by glacial-interglacial variability and by precession-controlled changes in the east-west thermocline slope of the Indo-Pacific. The precession-controlled variations in productivity are linked to processes similar to the Southern Oscillation phenomenon, and they precede changes in the oxygen isotopic ratio, which indicates that they are not the result of ice sheet fluctuations. The 30,000-year spectral peak in the tropical Indo-Pacific Ocean productivity records is also present in the Antarctica atmospheric CO_2 record, suggesting an important role for equatorial biological productivity in modifying atmospheric CO_2.

Interannual variability of the thermocline depth is a characteristic feature of the equatorial Pacific Ocean that has a strong influence on oceanic primary production (*1*). Most of the time, the tropical trade winds transport surface waters westward. This lifts the ther-